Hydrol. Earth Syst. Sci. Discuss., 10, 6019–6048, 2013
www.hydrol-earth-syst-sci-discuss.net/10/6019/2013/
doi:10.5194/hessd-10-6019-2013

Hydrology and Earth System Sciences
Open Access
Discussions

Spatial patterns in timing of the diurnal temperature cycle

T. R. H. Holmes[1], **W. T. Crow**[1], **and C. Hain**[2]

[1]USDA-ARS Hydrology and Remote Sensing Lab, Beltsville, MD, USA
[2]Earth System Science Interdisciplinary Center, University of Maryland, College Park, Maryland, USA

Received: 9 April 2013 – Accepted: 16 April 2013 – Published: 15 May 2013

Correspondence to: T. R. H. Holmes (thomas.holmes@ars.usda.gov)

Published by Copernicus Publications on behalf of the European Geosciences Union.

Abstract

This paper investigates the structural difference in timing of the diurnal temperature cycle (DTC) over land resulting from choice of measuring device or model framework. It is shown that the timing can be reliably estimated from temporally sparse observations acquired from a constellation of low Earth orbiting satellites given record lengths of at least three months. Based on a year of data, the spatial patterns of mean DTC timing are compared between Ka-band temperature estimates, geostationary thermal infrared (TIR) temperature estimates and numerical weather prediction model output from the Global Modeling and Assimilation Office (GMAO). It is found that the spatial patterns can be explained by vegetation effects, sensing depth differences and more speculatively the orientation of orographic relief features. In absolute terms, the GMAO model puts the peak of the DTC on average at 12:50 local solar time, 23 min before TIR with a peak temperature at 13:13. Since TIR is the shallowest observation of the land surface, this small difference represents a structural error that possibly affects the models ability to assimilate observations that are closely tied to the DTC. For non-desert areas, the Ka-band observations have only a small delay of about 15 min with the TIR observations which is in agreement with their respective theoretical sensing depth. The results of this comparison provide insights into the structural differences between temperature measurements and models, and can be used as a first step to account for these differences in a coherent way.

1 Introduction

In recent decades, Earth observation by satellite has progressed from experimental to routine methods for monitoring many aspects of the hydrological cycle over land. For example, cloud water and precipitation from satellite sensors are now routinely ingested into numerical weather prediction (NWP) models (Bauer et al., 2011). Soil moisture observations are at the point of entering into operational NWP assimilation

HESSD
10, 6019–6048, 2013

schemes (Rosnay et al., 2011). Indirect observations of the evaporative fluxes are now informing drought monitoring (Anderson et al., 2011; Hain et al., 2011). However, one crucial parameter that is missing from this list is land surface temperature (LST). Even though it has been routinely measured since the first Earth observation satellites, and physical-based retrieval schemes for the above parameters must account for LST in some way, it has yet to be successfully exploited as a stand-alone input to NWP models. This is striking since LST is tightly linked (even more so than soil moisture) to land-atmosphere fluxes that are a primary prediction goal for land models within NWP systems (Bosilovich et al., 2007).

The utilization of LST observations for hydrological studies is hampered by the fact that the relationship between different model and remotely-sensed based estimates of LST are poorly understood. This is because temperature is highly variable in time and space (both vertically and laterally). While, for example, soil moisture can be assumed diurnally stable, and an observation at midnight can readily be compared to another at 6 a.m. (Parinussa et al., 2012), it is obvious that no such assumption would hold for LST. The variability with depth is a problem when comparing temperature observations from different measurement techniques that have different sensing depths (and/or models which utilize different soil layers and/or soil thermal capacities). This variability with depth together with a high spatial variability poses a challenge to in situ validation of LST, even though thermal infrared (TIR) measuring techniques can have high spatial resolutions (up to 1 km for global MODIS products for example). An additional complication specific to the assimilation of LST is that in many NWP models the LST predictions have numerous structural errors. In previous attempts at assimilation of temperature observations into land surface models (Bosilovich et al., 2007; Reichle et al., 2010), these issues were addressed through rescaling of observations to match the auto-correlation and/or diurnal LST properties of models. While this may be the preferred strategy in a data assimilation approach where the physics of the model has to be preserved, it squanders the opportunity to correct structural errors in the surface energy balance via comparison to satellite LST observations. This is really a missed

HESSD
10, 6019–6048, 2013

opportunity because NWP centers are known to have diurnal biases in high-value predictions like precipitation (Dai and Trenberth, 2004).

In a comparison of temperature output from three different NWP models with in situ measurements, the depth difference between model and in could be resolved by considering the timing, or phase, (ϕ) of the diurnal temperature cycle (DTC) (Holmes et al., 2012). It was shown that based on the annual average difference between ϕ of measurements from different depths, the effect of 5 cm depth difference could accurately be corrected for. The logic behind this is that the difference in timing between two measurement or model systems represents the integrated effect of both depth difference and soil thermal properties. This timing difference is then assumed to be accompanied by an exponential change in amplitude according to heatflow principles (Van Wijk and de Vries, 1963).

Determining ϕ is relatively straightforward when the sampling frequency is much higher than the daily harmonic being sampled. This is true for NWP models, and also for observations from geostationary satellites. However, for a single satellite in low Earth orbit the sampling frequency at any location is much lower: 1–2 observations per day (depending on the swath width). For such satellites we need to combine the observations from multiple platforms in order to reliably estimate ϕ. This was shown in Holmes et al. (2013), where vertical polarized Ka-band observations from four platforms where combined before determining the Ka-band ϕ. That paper showed that Ka-band observations can be used to enhance NWP temperature output, but only if the temperature series are properly reconciled in terms of timing, amplitude, and minimum of the diurnal temperature cycle. In the near future, the potential sampling of the DTC by Ka-band sensors will be greatly enhanced by the constellation of satellites that will be launched under the auspices of the Global Precipitation Measurement mission (Smith et al., 2007). In this paper we determine ϕ of MERRA surface temperature data with an hourly output interval. We compare this to the ϕ as determined from a merged record of Ka-band brightness temperatures from six satellite platforms. As a third independent data source we use thermal infrared (TIR) LST retrievals from the

HESSD
10, 6019–6048, 2013

geostationary Meteosat-9 satellite (centered at a longitude of 0°), covering Europe and Africa.

When considered as group, these three sources (i.e., NWP-based, microwave-based and TIR-based) all provide independent information regarding LST and can theoretically be integrated together (via e.g. the assimilation of TIR and microwave LST observations into the NWP model) or used to improve physical retrievals methods for ET and soil moisture which require ancillary LST information. However, before these overarching goals can be accomplished, systematic differences in each LST data sets – particularly as they relate to ϕ – must be understood. This will not only support efforts to combine temperature from different sources, but may also help to better tailor a given temperature set to its function within physical retrieval models. For soil moisture remote sensing it may help to better adjust the temperature measurement to the sensing depth of the band that is actually used for the soil moisture retrieval. For precipitation, it may help efforts to improve the estimation of background emissivity estimation (Stephens and Kummerow, 2007). And finally, a proper reconciliation of thermal and microwave based temperature may improve evaporation models, such as ALEXI (Anderson et al., 1997), that currently depend on suboptimal gap-filling when clouds prevent TIR observations.

In preparation for a global merging of temperature data, this paper presents a global analysis of difference in DTC timing between Ka-band temperature estimates, TIR-based temperature estimates and NWP model output. The results of this comparison provide insights into the structural differences between temperature measurements and models, and can be used as a first step to account for them in a coherent way.

2 Theory

The time between solar noon and the time of the daily maximum is here referred to as the phase of the DTC (ϕ) and measured in hours. Because solar noon is the time of day when the sun is at its highest point in the sky for a given location, this local definition

HESSD
10, 6019–6048, 2013

eliminates any longitudinal dependency but also the smaller effect of variations in day length through the year. Accordingly, all times denoted here are given in local solar time.

For a surface temperature measurement, the average ϕ should be directly related to the incoming radiation, with a delay (damping) that is a function of heat capacity of the soil or vegetation layer over the measurement depth of the sensor. When comparing two temperature measurements with the same spatial extent, the measurement depth will determine the level of damping of the diurnal temperature cycle (Van Wijk and de Vries, 1963) and the measurement with the earliest peak will represent the shallowest layer. TIR measurements have a sensing depth of about 50 µm, providing the shallowest practical measurement of LST. The timing of the maximum TIR temperature is typically reported between 60–90 min after solar noon (Choudhury et al., 1987; Betts and Ball, 1995; Fiebrich et al., 2003). Ka-band microwave emission has been shown to be a plausible alternative to TIR measurements, with much higher tolerance for clouds but a limited spatial resolution (Holmes et al., 2009). The sensing depth for Ka-band microwave emission is slightly deeper than TIR and varies with soil moisture. For most land surfaces it is assumed to be around 1 mm. Accordingly, the ϕ derived from Ka-band emission is expected to be slightly behind that observed using TIR. Only in very dry areas with no vegetation is the Ka-band sensing depth potentially much deeper, in the order of cm's (Ulaby et al., 1986), and the ϕ of Ka-band can be even more delayed. To illustrate the difference, a numerical example is given in Table 1 comparing a wet soil to a dry soil. The damping of the temperature harmonic with a period of a day can be described by a phase shift ($\mathrm{d}\phi$) proportional to the vertical distance ($\mathrm{d}z$) divided by the damping depth (z_D). The damping depth is defined as the $\mathrm{d}z$ over which the amplitude of the harmonic is reduced by 63 %, and is an expression of the thermal properties of the soil:

$$z_\mathrm{D} = \sqrt{\frac{2a}{2\pi f}} \tag{1}$$

HESSD
10, 6019–6048, 2013

where a is the thermal diffusivity ($m^2 s^{-1}$) and f is the frequency (s^{-1}) of the harmonic. For a dry soil ($a = 0.15\, e^{-6}$) Eq. (1) yields an estimate of $z_D = 6.5$ cm. Estimates of the temperature sensing depth (z_S) of 1 mm for a wet soil to 1 cm for a dry soil are given in Ulaby et al. (1986). The difference in z_S for microwave Ka-band emission between a dry sandy soil and a wet soil is therefore about 9 mm. Dividing this by the dry soil z_D of 6.5 cm equates to a 3 h 36 min shift in ϕ between the soil layers at the lower ends of these sensing depths ($d\phi z$). Because the shallower soil depths weigh more heavily in the measured emission, and they have larger diurnal amplitudes, they affect the timing of the DTC more strongly. Therefore, the shift in phase ($d\phi$) of actual measured Ka-band emission, originating from the entire soil profile, is estimated at a fourth of $d\phi z$: 54 min. Observational evidence of this $d\phi$ will be discussed in Sect. 5.

3 Materials

In this study we compare three independent land temperature measurements, two from satellite measurements and one based on a global NWP model. The satellite observations include a number of Ka-band sensors with global coverage, and TIR measurements from a geostationary satellite. All sets were available for the full year 2009 and are described below.

3.1 Satellite Ka-band brightness temperature

Vertical polarized Ka-band (37 GHz) brightness temperatures ($T_B^{Ka,V}$) observations are available from several satellites. For 2009 we acquired observations from the Advanced Microwave Scanning Radiometer on EOS (AMSR-E), the Special Sensor Microwave and Imager (SSM/I) and the Tropical Rainfall Measurement Mission (TRMM) Microwave Imager (TMI), and Coriolus-WindSat. Detailed sensor specifications are listed in Table 2. The coverage of all polar orbiting satellites is global, whereas the equatorial orbit of TMI extends from 39° N to 39° S. Each sensor has a different spatial

HESSD
10, 6019–6048, 2013

resolution and the location of the center of the footprint and its azimuth orientation varies between consecutive overpasses. To combine these observations, they are binned to a 0.25° regular global grid. This resolution was chosen based on the satellite with the coarsest resolution (SSM/I, see Table 2). The value for each grid cell is the mean of all observations with a footprint center within the boundaries of the cell. The inter-calibration of these five instruments makes use of the precessing nature of TRMM's equatorial orbit. This orbit was designed to sample the diurnal variation of tropical rainfall and results in regular overlap with all polar orbiting satellites, allowing for an inter-calibration of the satellites as described in Holmes et al. (2013).

Within the microwave spectrum, $T_B^{Ka,V}$ is the most appropriate frequency to retrieve LST as it balances a reduced sensitivity to soil surface characteristics with a relatively high atmospheric transmissivity (Colwell et al., 1983). In Holmes et al. (2009) it was further shown that an assumption of a constant land surface emissivity can be used to obtain LST estimates from Ka-band with relatively high sensitivity, if not absolute accuracy. For the purpose of this paper no conversion to physical temperature is needed since only the timing of the DTC is analysed here, not its amplitude. This means that for this paper the assumption of constant emissivity needs only to hold over the course of the day, and that there is no effect of absolute bias in LST on the analysis. Still, the linear relationship between Ka-band and LST does potentially break down under frozen soil conditions or during precipitation events. This leads to the formulation of two conditions for the Ka-band data: $T_B^{Ka,V} > 260\,\mathrm{K}$, and $\sigma^{Ka,V} < \mathrm{mean}(\sigma^{Ka,V})$, as explained in more detail in Holmes et al. (2013). The Ka-band temperature set is referred to in the following as T_{Ka}. An example of the resulting sampling of the combined T_{Ka} is given in Fig. 1 for three days in September 2009. In the same graph the NWP and infrared resource are shown, they are described below.

HESSD
10, 6019–6048, 2013

3.2 NWP surface temperature

The modeled temperature dataset was acquired from NASA's Global Modeling and Assimilation Office (GMAO) and their Modern Era Retrospective-analysis for Research and Applications (MERRA) (http://gmao.gsfc.nasa.gov/research/merra, Rienecker et al., 2011). MERRA products are generated using Version 5.2.0 of the GEOS-5 DAS (Goddard Earth Observing System (GEOS) Data Assimilation System (DAS)) with the analysis and model output both at a spatial resolution of 0.5° latitude by 0.67° longitude, and with a 6 hourly analysis cycle. Two dimensional diagnostics describing the radiative and physical state of the surface are available as hourly averages.

Surface processes in MERRA are based on the NASA Catchment land surface model (Ducharne et al., 2000; Koster et al., 2000). Each MERRA grid cell contains several irregularly shaped tiles, and each tile is further divided into sub-tiles based on their modeled hydrological state: saturated, unsaturated, and wilting. The surface temperature of a grid cell is obtained by area-weighted averaging of the surface temperatures of all sub-tiles within the grid cell. The sub-tile surface temperatures are prognostic variables of the model and represent a bulk surface layer with a small but finite heat capacity. For all vegetation classes except broadleaf evergreen trees, this bulk surface layer represents the vegetation canopy and a surface layer at the top of the soil column (effective layer depth < 1 mm).

In this study we analyzed the gridded surface temperatures over land, or T_{NWP}. The data was regridded onto a 0.25° regular grid by means of bilinear interpolation, and the hourly output was temporally interpolated to a 15 min temporal resolution. Figure 1 gives an example of T_{NWP} at the original hourly resolution.

3.3 Geostationary thermal infrared based LST

TIR-based land surface temperature from METEOSAT-9 with coverage over Africa and Europe was available as a third independent data source. LST (T_{IR}) is an operational product of the Land Surface Analysis-Satellite Applications Facility (LSA-SAF,

HESSD
10, 6019–6048, 2013

see http://landsaf.meteo.pt). It is generated using spinning enhanced visible and infra red imager (SEVIRI) split-window channels (10.8 and 12.0 µm) on board the geostationary Meteosat second generation (MSG) satellite; therefore a high temporal resolution (15 min) of the data is possible (Kabsch et al., 2008; Trigo et al., 2011).

This LST data is provided on a 3-km equal area grid. When regridding onto a 0.25° regular grid, this results in a large over sampling of the grid box. If more than two-thirds of the 3-km observations are masked out for a particular location and time, then that sampling average is rejected. This threshold increases the amount of data discarded by the cloud filter for T_{IR}. We further limit the coverage of the METEOSAT-9 to the domain covered with an Earth incidence angle of 78°, avoiding artifacts at large view angles. In Fig. 1 the high sampling rate of T_{IR} is apparent, as are gaps (attributed to clouds) on day 1 and 2 of this example series.

4 Methods

In Holmes et al. (2012) it was shown that a relative estimate of ϕ can be determined by fitting a simple harmonic model to a temperature time-series. This worked well enough when only ϕ differences between temperature sets are needed. However, the values itself are hard to interpret since the actual shape of the DTC rarely resembles a perfect harmonic shape resulting in differences between the time of maximum temperature and the peak of the harmonic.

In this paper we adapt a more sophisticated model of the DTC as described by Göttsche and Olesen (2001). This harmonic-exponential DTC model improves the fit along the cooling limb of the DTC and allows for better leveraging of observations at all times. In addition, it yields an estimate of ϕ that can be more readily interpreted as the time-lag between solar noon and peak temperature. The DTC model by Göttsche and Olesen (2001) is originally intended as a five parameter model, and a subsequent addition to parameterize total (atmospheric) optical depth increased this to six (Göttsche and Olesen, 2009). A recent comparison paper (Duan et al., 2012) discussed several

HESSD
10, 6019–6048, 2013

variants of the DTC model by Göttsche and Olesen (2001) and showed that improvements were caused by adding an additional free parameter related to the day-length. In this paper we have to reduce the number of free parameters to limit the computational demands and speed conversion to a solution. Therefore we simplify the five parameter model (Göttsche and Olesen, 2001) to have only three free parameters. A test shows that this does not reduce the accuracy of the mean ϕ as determined over longer time series. The method is detailed below.

In Göttsche and Olesen (2001) the DTC model (T_{par}) is parameterized as a function of the time of maximum (t_m), day length (ω), diurnal amplitude (T_a), diurnal minimum (T_0), change in minimum from day to day (δT), and start of the attenuation function (t_s):

$$T_{par}(t) = T_0 + T_a \cos\left(\frac{\pi}{\omega}(t - t_m)\right), \quad t < t_s \tag{2}$$

$$T_{par}(t) = T_0 + \delta T + \left[T_a \cos\left(\frac{\pi}{\omega}(t_s - t_m)\right) - \delta T\right] e^{\frac{-(t-t_s)}{k}}, \quad t \geq t_s$$

Figure 2 shows an example of T_{par}, and illustrates the definitions of its parameters. The attenuation constant k is calculated by making the first derivatives of the day and night time equation equal at time t_s:

$$k = \frac{\pi}{\omega}\left[\frac{1}{\tan\left(\frac{\pi}{\omega}(t_s - t_m)\right)} - \frac{\delta T}{T_a \sin\left(\frac{\pi}{\omega}(t_s - t_m)\right)}\right] \tag{3}$$

To limit the degrees of freedom and increase conversion to a solution, in this study the start of the attenuation function is fixed so that half of the decrease in temperature (over the cooling down limb) is described by the exponential equation. That way, t_s can be calculated from t_m and ω as:

$$t_s = t_m + \frac{\omega}{\pi}\arccos\left(\frac{1}{2}\left(1 + \frac{\delta T}{T_a}\right)\right) \tag{4}$$

For a given day and temperature set, first guess estimates of T_0 and T_a are determined based on the minimum and maximum recorded observations within the 24 h

HESSD
10, 6019–6048, 2013

period from sunrise to sunrise. Similarly, δT is initialized based on the difference between T_0 of the current and the next day, if available. Solar noon (t_n) and ω are calculated based on latitude and day of year according to general solar position calculations Cornwall et al. (2003). Defining ϕ as the offset between optimized time of maximum temperature and sunrise $t_m = t_n + \phi$, there are three free parameters: ϕ, T_0, T_a. Of these, only T_0, T_a, vary from day to day, ϕ is assumed constant over the data range. With these assumptions it is possible to determine ϕ in an iterative optimization loop that minimizes the squared errors (E) between T_{par} and the data series. In Fig. 1 examples of T_{par} are shown, as fitted for the three LST resources used in this manuscript.

The timing of the DTC can be determined if temperature observations are available with a sufficient sampling, which at minimum includes samples near the time of minimum and maximum temperature and at mid morning and afternoon. Furthermore, days (d) where one of the following conditions are not met are removed from the timing fitting to assure that the basic assumptions of the temperature model are not violated:

1. $T_0(d)$ above freezing point,
2. $t_m(d)$ within 2 h of mean t_m,
3. $T_a > 5$ K, and
4. $N(d) > \text{median}(N(d = 1 : \text{end}))$.

The first condition is used to avoid days with subfreezing temperatures because the Ka-band/LST relationship weakens under these circumstances, and the second assures that the DTC has a shape close to the clear sky assumptions. The third condition is intended to make sure the signal to noise ratio is acceptable. The last condition tests that the sampling of the DTC is not much less than on the average day ($N(d)$ is the number of datapoints in LST at day d).

The fitting of the timing is dependent on the sampling of the series. To test if the sampling of T_{Ka} results in a bias relative to the hourly sampling of MERRA, we looked at the change in apparent timing for T_{NWP}, when only observations at the overpass times

HESSD
10, 6019–6048, 2013

of the Ka-band set are used. The effect of sparse sampling on the ϕ is averaged by latitude and shown in Fig. 3. The effect was no greater than 9 min for 99 % of the data, although on average the sparse sampling resulted in 2 min positive bias of ϕ. These results indicate that the uncertainty as introduced by the limited sampling frequency of the Ka-band data is small enough to measure Ka-band timing from this set of sensors.

5 Results

The above described method to determine ϕ is applied to the three temperature records T_{Ka}, T_{NWP}, and T_{IR} (described in Sect. 3) for the data year 2009. The resulting (0.25°) maps of ϕ are displayed in Fig. 4 for Europe and Africa, the spatial domain of MSG-9.

On average the T_{Ka} peaks at 13:44 with lower values over Europe and highest values over deserts and tropical rainforests. Later values of peak temperature in deserts can be explained by the deeper sensing depth of Ka-band emission under dry soil conditions (see Sect. 2). In fact, the areas with latest ϕ correspond closely to sand deserts, see for example the Arabian Peninsula in Fig. 4a where the Rub'al Khali Erg shows up causing an hour delay of the Ka-band ϕ. This feature was earlier noted in terms of day/night difference of SSM/I channels (Prigent et al., 1999), polarization difference of AMSR-E channels (Jiménez et al., 2010), and even more comparable to the present analysis, in terms of phase difference between microwave and TIR temperature (Norouzi et al., 2012). In this later study the third component derived from a principal component analysis (PCA) was attributed to the phase of the diurnal cycle. The close resemblance of the spatial features generally supports this conclusion.

Another feature in the maps of $\phi(T_{Ka})$ is the earlier phase over mountainous areas (e.g. the Rif mountains in NW Africa, Caucasus). Since T_{Ka} is composed of observations with varying azimuth angles, the signature likely reflects a deviation in actual maximum insolation relative to the calculated solar noon, but a detailed investigation is beyond the scope of this paper.

HESSD
10, 6019–6048, 2013

For T_{NWP}, with a mean peak temperature at 12:50, there is much less spatial variation in ϕ with the notable exception of tropical rainforest, see Fig. 4b. The distinctly different results over rainforest with values around 13:30 are explained by a higher heat capacity as parameterized for areas classified as tropical forest in the MERRA model. At more northern latitudes, higher ϕ-values are found over the forest areas of the East-European plain.

Figure 4c shows the ϕ as determined based on T_{IR}. The T_{IR} data peak on average at 13:13. The higher ϕ-values in the tropical zone match well with the delay as found for T_{NWP}, although for T_{IR} the area with delayed ϕ is slightly more expansive and includes more generally the humid tropical zone of Africa.

Figure 4d shows a North South transect of the ϕ as determined for T_{Ka}, T_{NWP}, and T_{IR}; all averaged over the longitude extent of 0–30° E. All sets have a delayed ϕ around the equator, which for T_{NWP} is explained by the higher heat-capacity as parameterized for tropical rainforest. For T_{Ka} and T_{IR}, with little to none penetration of the canopy layer, the delay in ϕ might more plausibly have to do with the effect of a diurnal pattern in cloudiness which can cause a delay in the peak solar radiation. Superimposed on this tropical signature, T_{Ka} clearly shows a delayed ϕ over (seasonally) dry areas in Northern and Southern Africa, explained by the deeper sensing depth.

Some of the patterns in ϕ and differences between the sets seem to align with particular land surface types. Therefore, MODIS land cover maps (MCD12C1, Version 051) are used to study ϕ by land surface type (International Geosphere-Biosphere Programme (IGBP) classification). Figure 6 lists the average values as obtained over selected surface types between longitudes 0 to 30° E. This indeed confirms the general relation with vegetation type; both T_{IR} and T_{NWP} exhibit delayed ϕ over broadleaf forest compared to all other land surface types. As a consequence, the mean difference in ϕ is remarkably homogenous: $\phi(T_{IR}) - \phi(T_{NWP}) = 27$ min (± 15 min) for 79 % of the land area. Areas with larger differences are found at the edge of land masses where $\phi(T_{IR})$ can be up to 1.5 h behind $\phi(T_{NWP})$ as shown in Fig. 5. This is apparently related to T_{IR} exhibiting a delay in ϕ relative to the interior of the continents (see also Fig. 4c). Since

HESSD
10, 6019–6048, 2013

these features appear to line up with the mountain ranges, with delayed ϕ over ranges that are to the East of MSG-9, and earlier ϕ over mountains to the North-West of the satellite, it is tentatively attributed to orographic effects as described in Senkova et al. (2007).

Although T_{Ka} closely matches T_{IR} in terms of ϕ for the forest and cropland cover types, an additional delay is recorded over the dry areas of the world, as is evident in Figs. 4 and 6. The resulting timing difference between T_{Ka} and T_{IR} is therefore greatest over the driest parts of Africa, where T_{Ka} is 57 min (±25 min) behind T_{IR} in ϕ, see Fig. 5b. This average dϕ agrees with the theoretical calculations of Sect. 4. This suggests that the large increase in ϕ_{Ka} over dry areas can be quantitatively explained by the increase in temperature sensing depth. As expected for all but the driest soils (especially when covered with vegetation) the difference is much closer to zero over the rest of Africa and Europe. For example, over Europe the ϕ-maps show that T_{Ka} is only 14 min (±12 min) behind T_{IR}. In some coastal and mountainous areas the ϕ-maps indicate that T_{Ka} peaks earlier than T_{IR}, which is not physically realistic. Most of these areas also show up in the previous discussion of Fig. 5a, and are attributed to a delay in T_{IR} that has yet to be fully explained. It is most likely related to a failure of the cloud mask applied to TIR. In addition to those areas however, T_{Ka} appears to be ahead of T_{IR} over Turkey and this is likely caused by T_{Ka}, which has anomalous early ϕ there (see Fig. 4a). The difference in ϕ between T_{Ka} and T_{NWP} will be discussed in a global context in the next section.

It is investigated if these patterns in ϕ are stable through the year. For that the above procedure was repeated for 3 month seasonal periods. For T_{Ka} and T_{NWP} no differences with the annual ϕ were found larger than 15 min. For T_{IR} the northern sub-tropical zone showed delayed ϕ of up to a half hour, but this is likely related to a lack of sufficient days with clear sky conditions.

HESSD
10, 6019–6048, 2013

6 Global results

This section will briefly discuss the global maps of ϕ as generated for T_{Ka} and T_{NWP}. The geostationary TIR resource is not yet available as a consolidated global dataset and is therefore not included here.

The global maps of ϕ confirm the land-cover features as discussed above. The T_{Ka} peaks on average at 13:37 (see Fig. 7, top), but over desert areas this peak is up to an hour delayed. For T_{NWP} (Fig. 7, middle panel), ϕ is generally between 12:30 and 13:00 with two main exceptions, the tropical regions and Northern latitudes. Highly delineated areas appear in the tropical zone with a delay in ϕ of up about 40 min. As discussed earlier, this is explained by the increased heat capacity of the surface layer as parameterized for tropical forest by MERRA. Because this is a static feature of MERRA, the resulting spatial pattern of ϕ is expected to remain stable from year to year, as long as the same land classification is used. Above 60° N delays of up to an hour are calculated (e.g. Alaska, Scandinavia, Siberia) possibly resulting from frozen circumstances and a less pronounced diurnal temperature range.

On average T_{Ka} peaks 40 min later than T_{NWP} (Fig. 7, lower pane). In the temperate climates and the tropics the dϕ is close to this average. Bigger differences appear in the desert areas where Ka-band peaks up to 2 h after T_{NWP}, corresponding to a deeper sensing depth. The Northern latitudes show smaller differences due to the delayed ϕ of T_{NWP}, a feature that is not matched in T_{Ka}. Due to the close link with land cover and geological features it is expected that these patterns of dϕ would largely remain stable from year to year.

7 Conclusions

This study has demonstrated that the timing of the diurnal temperature cycle can reliably be determined from temporally sparse datasets. The method is applied to a year-long record of geostationary TIR observations, model output, and a combination of low

HESSD
10, 6019–6048, 2013

Earth orbiting satellites with microwave radiometers. The spatial patterns in ϕ for each temperature set are explainable based on consideration of land surface type and basic physics describing the penetration depth of microwave observations. An interesting observation is that over tropical forest the timing is delayed by 30 to 40 min relative to the average phase in both satellite data sets. While this delay is accurately modeled in MERRA, it may be for the wrong reason if the delay is caused by a diurnal variability of cloudiness rather than an increase in heat capacity of the sampled surface layer. On the other hand, deserts cause a delay in the timing of Ka-band diurnal temperature cycle that is not matched in the TIR nor MERRA estimates. This is explained by a deeper sensing depth for the microwave observations in dry soils, and becomes especially extreme in dry sand deserts.

In absolute terms, MERRA seems to model the peak of the DTC about 23 min before that of TIR, which should be the shallowest observation possible of the land surface. Therefore, if the goal is to model the surface temperature it appears the heat capacity of the surface layer is set slightly too low in MERRA. The timing of Ka-band observations outside of the desert areas is on average 15 min after TIR. This small delay of the DTC compared to TIR agrees with a slightly deeper sensing depth for Ka-band, 50 µm vs. 1 mm.

This study has identified structural differences in diurnal timing between MERRA, TIR and Ka-band based land surface temperature estimates and constitutes one of the first global analyses of the effects of vegetation and sensing depth on the timing of different temperature measurements. Even though the global maps of the timing for each set are based on the year 2009, these features are expected to be relatively stable from year to year. With these maps we can now attempt to adjust for these structural differences in temperature estimates and study the relative merit of each method in a more consistent way.

Acknowledgements. This work was funded by NASA through the research grant "The Science of Terra and Aqua" (NNH09ZDA001N-TERRAQUA). The authors would like to thank the Global Modeling and Assimilation Office (GMAO) and the GES DISC (both at NASA Goddard Space

HESSD
10, 6019–6048, 2013

Flight Center) for the dissemination of MERRA. USDA is an equal opportunity provider and employer.

References

Anderson, M. C., Norman, J. M., Diak, G. R., Kustas, W. P., and Mecikalski, J. R.: A two-source time-integrated model for estimating surface fluxes using thermal infrared remote sensing, Remote Sens. Environ., 60, 195–216, 1997. 6023

Anderson, M. C., Hain, C., Wardlow, B., Pimstein, A., Mecikalski, J. R., and Kustas, W. P.: Evaluation of drought indices based on thermal remote sensing of evapotranspiration over the continental United States, J. Climate, 24, 2025–2044, doi:10.1175/2010jcli3812.1, 2011. 6021

Bauer, P., Auligné, T., Bell, W., Geer, A., Guidard, V., Heilliette, S., Kazumori, M., Kim, M. J., Liu, E. H. C., and McNally, A. P.: Satellite cloud and precipitation assimilation at operational NWP centres, Q. J. Roy. Meteor. Soc., 137, 1934–1951, 2011. 6020

Betts, A. K. and Ball, J. H.: The FIFE surface diurnal cycle climate, J. Geophys. Res.-Atmos., 100, 25679–25693, 1995. 6024

Bosilovich, M. G., Radakovich, J. D., da Silva, A., Todling, R., and Verter, F.: Skin temperature analysis and bias correction in a coupled land-atmosphere data assimilation system, J. Meteorol. Soc. Jpn., 85, 205–228, 2007. 6021

Choudhury, B. J., Idso, S. B., and Reginato, R. J.: Analysis of an empirical model for soil heat flux under a growing wheat crop for estimating evaporation by an infrared-temperature based energy balance equation, Agr. Forest Meteorol., 39, 283–297, 1987. 6024

Colwell, R. N., Simonett, D. S., and Ulaby, F. T. (Eds.): Manual of remote sensing, in: Interpretation and Applications, 2nd Edn., vol. II, Falls Church, 1983. 6026

Cornwall, C., Horiuchi, A., and Lehman, C.: General solar position calculations., available at: http://www.esrl.noaa.gov/gmd/grad/solcalc/solareqns.PDF (last access: May 2013), 2003. 6030

Dai, A. and Trenberth, K. E.: The diurnal cycle and its depiction in the Community Climate System Model, J. Climate, 17, 930–951, doi:10.1175/1520-0442(2004)017<0930:TDCAID>2.0.CO;2, 2004. 6022

HESSD
10, 6019–6048, 2013

Duan, S.-B., Li, Z.-L., Wang, N., Wu, H., and Tang, B.-H.: Evaluation of six land-surface diurnal temperature cycle models using clear-sky in situ and satellite data, Remote Sens. Environ., 124, 15–25, 2012. 6028

Ducharne, A., Koster, R., Suarez, M., Stieglitz, M., and Praveen, K.: A catchement-based approach to modeling land-surface processes in a GCM – 2. Parameter estimation and model demonstration, J. Geophys. Res., 105, 24809–24822, 2000. 6027

Fiebrich, C. A., Martinez, J. E., Brotzge, J. A., and Basara, J. B.: The Oklahoma Mesonet's Skin Temperature Network, J. Atmos. Ocean. Tech., 20, 1496–1504, doi:10.1175/1520-0426(2003)020<1496:TOMSTN>2.0.CO;2, 2003. 6024

Göttsche, F.-M. and Olesen, F. S.: Modelling of diurnal cycles of brightness temperature extracted from METEOSAT data, Remote Sens. Environ., 76, 337–348, 2001. 6028, 6029

Göttsche, F.-M. and Olesen, F.-S.: Modelling the effect of optical thickness on diurnal cycles of land surface temperature, Remote Sens. Environ., 113, 2306–2316, 2009. 6028

Hain, C. R., Anderson, M. C., Zhan, X., Svoboda, M., Wardlow, B., Mo, K., Meckalski, J. R., Kustas, W. P., and Brown, J.: A GOES Thermal-Based Drought Early Warning Index for NIDIS, in: NOAA's National Weather Service, Science and Techn. Inf. Climat. B., Fort Worth, TX, 2011. 6021

Holmes, T. R. H., De Jeu, R. A. M., Owe, M., and Dolman, A. J.: Land surface temperature from Ka band (37 GHz) passive microwave observations, J. Geophys. Res., 114, D04113, doi:10.1029/2008JD010257, 2009. 6024, 6026

Holmes, T. R. H., Jackson, T. J., Reichle, R. H., and Basara, J. B.: An assessment of surface soil temperature products from numerical weather prediction models using ground-based measurements, Water Resour. Res., 48, W02531, doi:10.1029/2011WR010538, 2012. 6022, 6028

Holmes, T. R. H., Crow, W. T., Yilmaz, M. T., Jackson, T. J., and Basara, J. B.: Enhancing model-based land surface temperature estimates using multiplatform microwave observations, J. Geophys. Res.-Atmos., 118, 1–15, 2013. 6022, 6026

Jiménez, C., Catherinot, J., Prigent, C., and Roger, J.: Relations between geological characteristics and satellite-derived infrared and microwave emissivities over deserts in northern Africa and the Arabian Peninsula, J. Geophys. Res., 115, D20311, doi:10.1029/2010JD013959, 2010. 6031

HESSD
10, 6019–6048, 2013

Kabsch, E., Olesen, F. S., and Prata, F.: Initial results of the land surface temperature (LST) validation with the Evora, Portugal ground-truth station measurements, Int. J. Remote Sens., 29, 5329–5345, doi:10.1080/01431160802036326, 2008. 6028

Koster, R., Suarez, M., Ducharne, A., Stieglitz, M., and Praveen, K.: A catchement-based approach to modeling land-surface processes in a GCM – 1. Model structure, J. Geophys. Res., 105, 24809–24822, 2000. 6027

Norouzi, H., Tenimi, M., AghaKouchak, A., Azarderakhsh, M., and Khanbilvardi, R.: On the effect of land cover type on the diurnal cycle of microwave brightness tmperatures, IEEE Geosci. Remote Sense., submitted, 2012. 6031

Parinussa, R. M., Holmes, T. R. H., and De Jeu, R. A. M.: Soil moisture retrievals from the WindSat spaceborne polarimetric microwave radiometer, IEEE Trans. Geosci. Remote, 50, 2683–2694, doi:10.1109/TGRS.2011.2174643, 2012. 6021

Prigent, C., Rossow, W. B., Matthews, E., and Marticorena, B.: Microwave radiometric signatures of different surface types in deserts, J. Geophys. Res., 104, 12147–12158, doi:10.1029/1999JD900153, 1999. 6031

Reichle, R. H., Kumar, S. V., Mahanama, S. P. P., Koster, R. D., and Liu, Q.: Assimilation of satellite-derived skin temperature observations into land surface models, J. Hydrol., 11, 1103–1122, doi:10.1175/2010JHM1262.1, 2010. 6021

Rienecker, M. M., Suarez, M. J., Gelaro, R., Todling, R., Bacmeister, J., Liu, E., Bosilovich, M. G., Schubert, S. D., Takacs, L., Kim, G.-K., Bloom, S., Chen, J., Collins, D., Conaty, A., da Silva, A., Gu, W., Joiner, J., Koster, R. D., Lucchesi, R., Molod, A., Owens, T., Pawson, S., Pegion, P., Redder, C. R., Reichle, R., Robertson, F. R., Ruddick, A. G., Sienkiewicz, M., and Woollen, J.: MERRA: NASA's Modern-Era Retrospective Analysis for Research and Applications, J. Climate, 24, 3624–3648, doi:10.1175/JCLI-D-11-00015.1, 2011. 6027

Rosnay, P. D., Drusch, M., Balsamo, G., Albergel, C., and Isaksen, L.: Extended Kalman Filter soil-moisture analysis in the IFS, ECMWF Newsletter, pp. 12–15, available at: http://www.ecmwf.int/publications/newsletters/pdf/127.pdf (last access: May 2013), 2011. 6021

Senkova, A. V., Rontu, L., and Savijarvi, H.: Parametrization of orographic effects on surface radiation in HIRLAM, Tellus A, 59, 279–291, doi:10.1111/j.1600-0870.2007.00235.x, 2007. 6033

Smith, E., Asrar, G., Furuhama, Y., Ginati, A., Mugnai, A., Nakamura, K., Adler, R., Chou, M. D., Desbois, M., and Durning, J.: International global precipitation measurement (GPM) program

HESSD
10, 6019–6048, 2013

and mission: an overview, in: Measuring Precipitation From Space, Springer, 611–653, 2007. 6022

Stephens, G. L. and Kummerow, C. D.: The remote sensing of clouds and precipitation from space: a review, J. Atmos. Sci., 64, 3742–3765, doi:10.1175/2006JAS2375.1, 2007. 6023

Trigo, I. F., Dacamara, C. C., Viterbo, P., Roujean, J. L., Olesen, F., Barroso, C., Camacho-de Coca, F., Carrer, D., Freitas, S. C., and Garcia-Haro, J.: The satellite application facility for land surface analysis, Int. J. Remote Sens., 32, 2725–2744, doi:10.1080/01431161003743199, 2011. 6028

Ulaby, F. T., Moore, R. K., and Fung, A. K.: From theory to applications, in: Microwave Remote Sensing: Active and Passive, vol. III, Artech House, Norwood, MA, 1986. 6024, 6025

Van Wijk, W. R. and de Vries, D. A.: Periodic temperature variations in a homogeneous soil, in: Physics of the Plant Environment, edited by: Van Wijk, W. R., North-Holland Publ. Co., Amsterdam, 102–143, 1963. 6022, 6024

HESSD

10, 6019–6048, 2013

Table 1. Soil thermal properties and phase shift examples.

	Wet soil	Dry soil
a: thermal diffusivity ($m^2 s^{-1}$)	$0.56e^{-6}$	$0.15e^{-6}$
z_D: damping depth (m)	0.124	0.064
z_S: sensing depth (m)	0.001	0.01
$d\phi z$: phase shift between deepest layers, wet to dry	$d\phi z = (z_{S,dry} - z_{S,moist})/z_D$ = (0.009/0.06) = 3 h 36 min	
$d\phi$: effective phase shift	$d\phi = d\phi z/4$ = 54 min	

HESSD
10, 6019–6048, 2013

Table 2. Specifications of satellite sensors providing Ka-band microwave observations used for land surface temperature estimation. (*AMSR2 was launched in May 2012.)

Sensor	SSM/I	TMI	AMSR-E	WindSat
Satellite	DMSP F13, F15	TRMM	Aqua	Coriolus
Orbit	Polar	Equatorial	Polar	Polar
Equatorial Overpass	6–10 a.m./p.m.	Variable	1.30 a.m./p.m.	6 a.m./p.m.
Operational	1987–present	1997–present	2002–2011*	2003–present
Accuracy (K)	0.4	0.5	0.7	0.5
Spatial Resolution (km)	33	10	12	12
Over-sampling in 0.25° grid	1	6	8	8

HESSD
10, 6019–6048, 2013

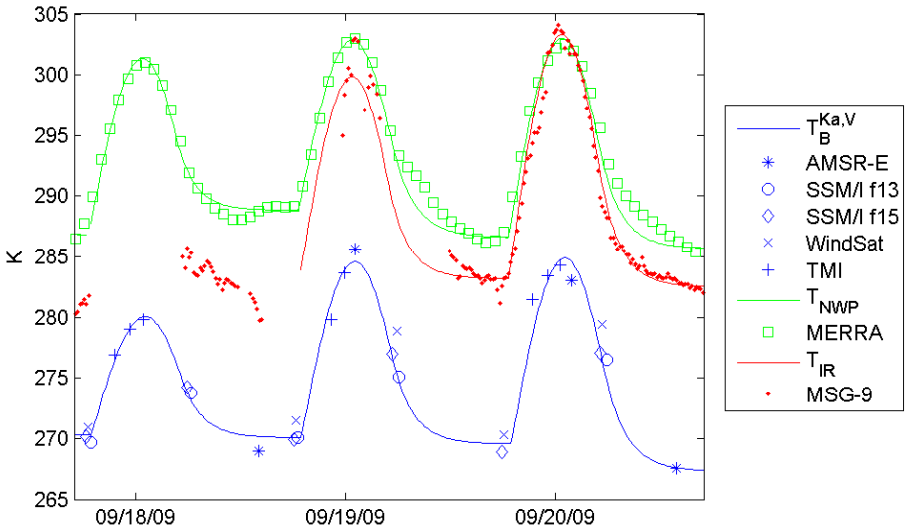

Fig. 1. Three days of diurnal cycles of T_{Ka}, T_{NWP}, and T_{IR} in September 2009. All variables are explained in Sect. 3. Solid lines represent the fitted DTC, as described in Sect. 4.

HESSD
10, 6019–6048, 2013

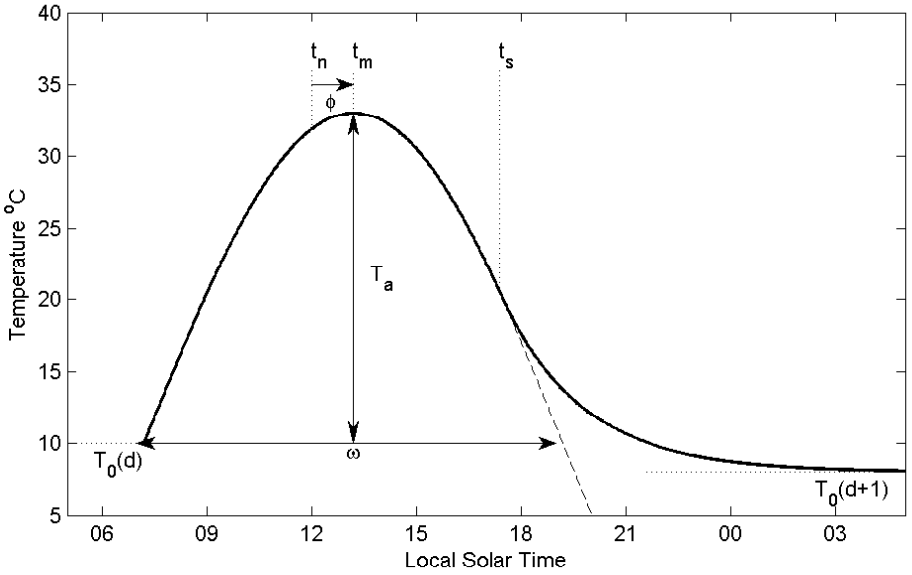

Fig. 2. Main characteristics of the diurnal temperature cycle, and the definition of the phase of the DTC (ϕ).

HESSD
10, 6019–6048, 2013

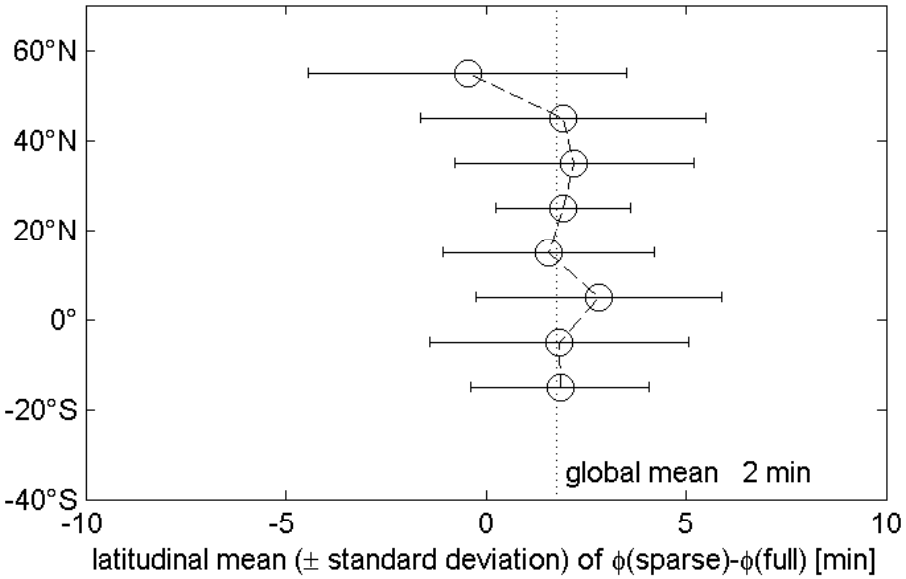

Fig. 3. Effect of sparse sampling on retrieval of ϕ, tested at T_{Ka} observation times.

HESSD
10, 6019–6048, 2013

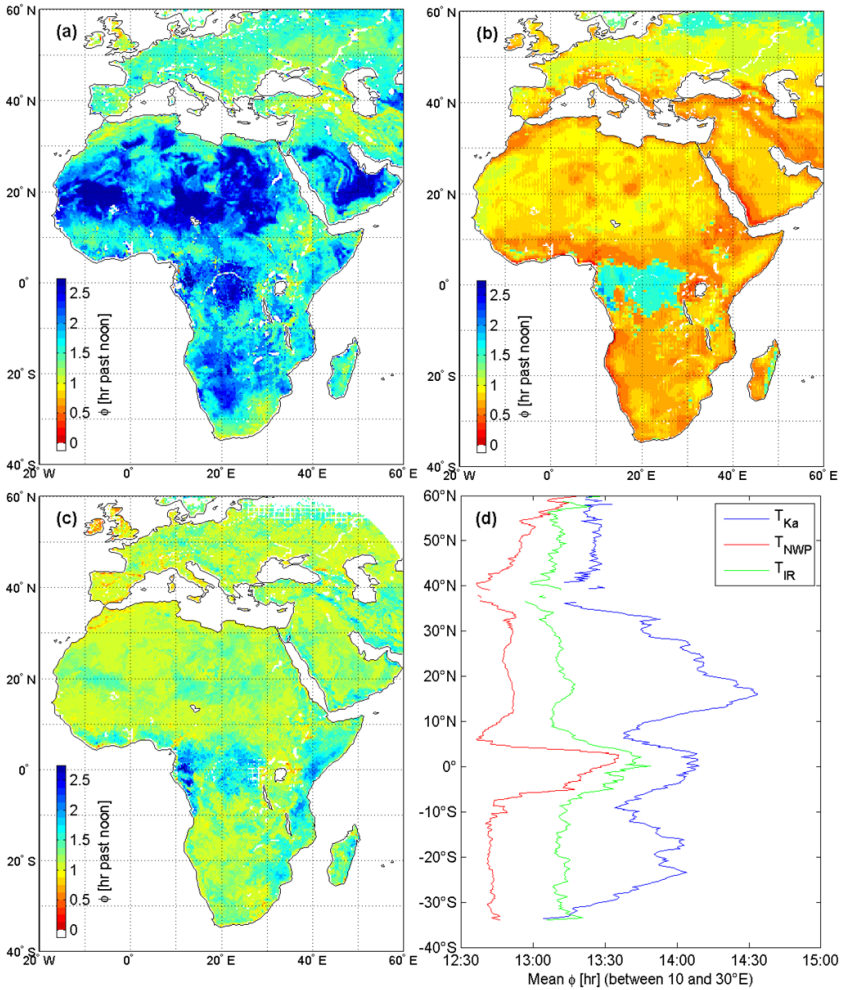

Fig. 4. 2009 mean ϕ for T_{Ka} **(a)**, T_{NWP} **(b)**, and T_{IR} **(c)**. **(d)** North south transect of mean ϕ.

HESSD
10, 6019–6048, 2013

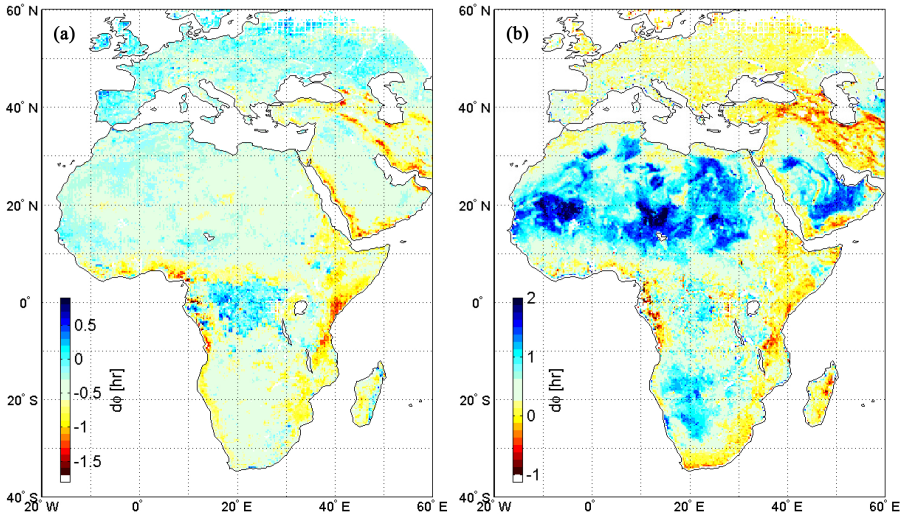

Fig. 5. Timing difference [h]: **(a)** $\phi(T_{NWP}) - \phi(T_{IR})$, average d$\phi$ = −23 min, and **(b)** $\phi(T_{Ka}) - \phi(T_{IR})$, average d$\phi$ = 30 min. Color bar centered on the average for each map.

HESSD
10, 6019–6048, 2013

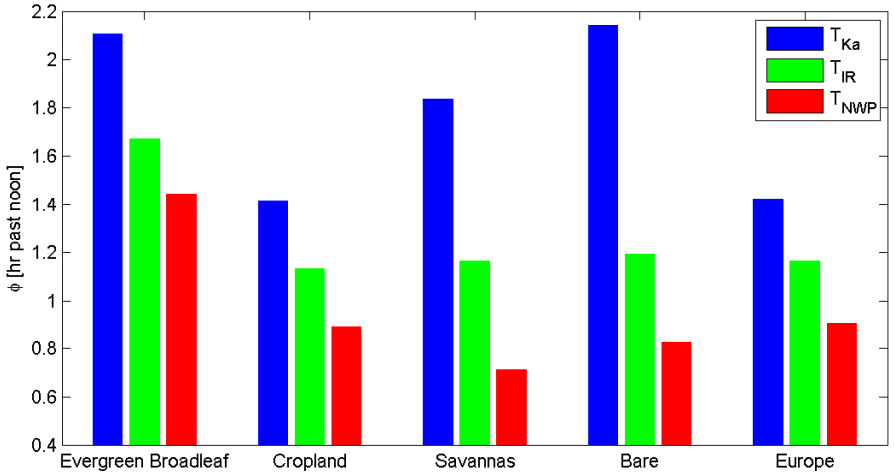

Fig. 6. 2009 mean ϕ determined for T_{Ka}, T_{IR}, and T_{NWP} for selected IGBP land-cover types. Between T_{NWP} and T_{IR} there is a fairly constant dϕ of 20 min. T_{Ka} agrees with T_{IR} over land surface types with little or no barren surface.

HESSD
10, 6019–6048, 2013

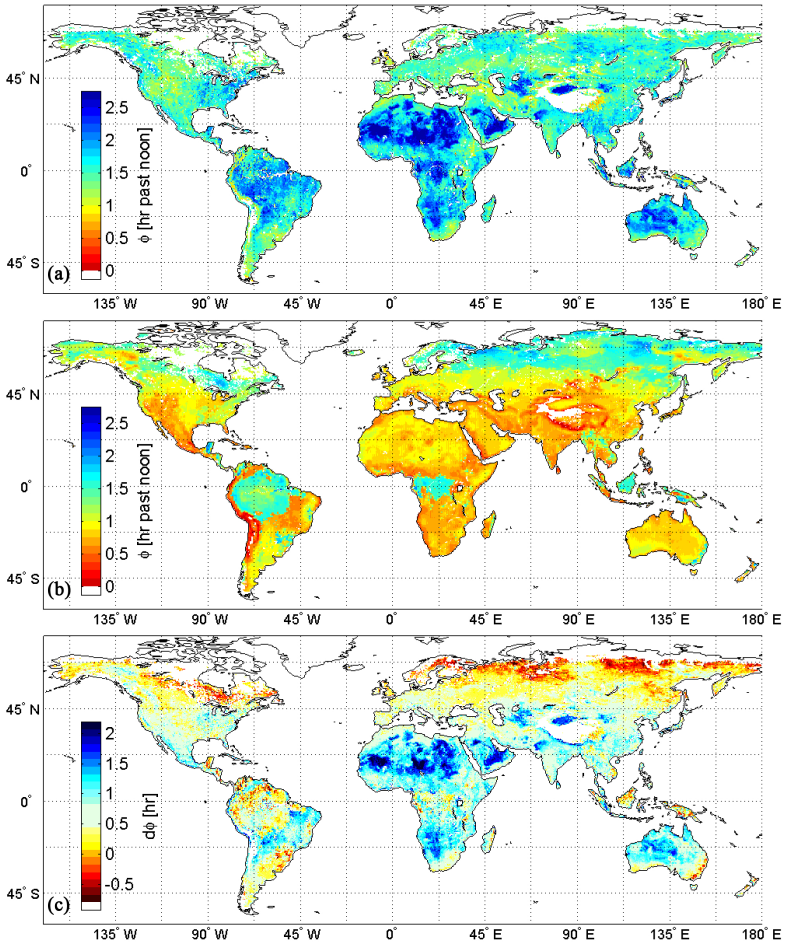

Fig. 7. 2009 mean ϕ for T_{Ka} **(a)**, T_{NWP} **(b)**, and difference $T_{Ka} - T_{NWP}$ **(c)**.

HESSD
10, 6019–6048, 2013